Electrically Tunable Valley-Light Emitting Diode (vLED) Based on CVD-Grown Monolayer WS$_2$

Weihuang Yang,[†,‡] Jingzhi Shang,[‡] Jianpu Wang,[§] Xiaonan Shen,[‡] Bingchen Cao,[‡] Namphung Peimyoo,[‡] Chenji Zou,[‡] Yu Chen,[‡] Yanlong Wang,[‡] Chunxiao Cong,[‡] Wei Huang,*[,†,§,‖] and Ting Yu*[,‡,⊥]

[†]Nanjing Tech Center of Research and Development, Nanjing Tech University, Nanjing 211816, People's Republic of China

[‡]Division of Physics and Applied Physics, School of Physical and Mathematical Sciences, Nanyang Technological University, Singapore 637371

[§]Key Laboratory of Flexible Electronics (KLOFE) and Institue of Advanced Materials (IAM), National Jiangsu Synergistic Innovation Center for Advanced Materials (SICAM), Nanjing Tech University (Nanjing Tech), 30 South Puzhu Road, Nanjing 211816, People's Republic of China

[‖]Key Laboratory for Organic Electronics and Information Displays (KLOEID) and Institute of Advanced Materials (IAM), Nanjing University of Posts and Telecommunications, Nanjing 210023, Jiangsu, People's Republic of China

[⊥]Department of Physics, Faculty of Science, National University of Singapore, Singapore 117542

S *Supporting Information*

ABSTRACT: Owing to direct band gap and strong spin−orbit coupling, monolayer transition-metal dichalcogenides (TMDs) exhibit rich new physics and great applicable potentials. The remarkable valley contrast and light emission promise such two-dimensional (2D) semiconductors a bright future of valley-tronics and light-emitting diodes (LEDs). Though the electro-luminescence (EL) has been observed in mechanically exfoliated small flakes of TMDs, considering real applications, a strategy that could offer mass-product and high compatibility is greatly demanded. Large-area and high-quality samples prepared by chemical vapor deposition (CVD) are perfect candidates toward such goal. Here, we report the first demonstration of electrically tunable chiral EL from CVD-grown monolayer WS$_2$ by constructing a p−i−n heterojunction. The chirality contrast of the overall EL reaches as high as 81% and can be effectively modulated by forward current. The success of fabricating valley LEDs based on CVD WS$_2$ opens up many opportunities for developing large-scale production of unconventional 2D optoelectronic devices.

KEYWORDS: WS$_2$, 2D semiconductor, chemical vapor deposition, light-emitting diode, valley polarization, chiral electroluminescence
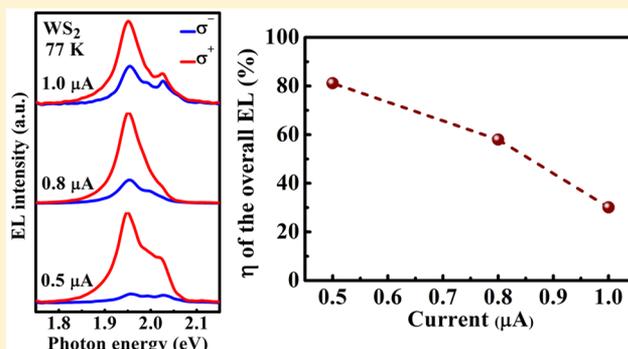
L ayered transition metal dichalcogenides (TMDs) have attracted rapidly growing scientific interest for next-generation electrical and optoelectronic device applications[1] owing to their unique physical, electrical, and optical properties. For an individual monolayer that consists of one atomic layer of transition-metal (typically Mo or W) sandwiched by two layers of chalcogen (typically S or Se), the band gap is significantly larger than that of its bulk due to the strong quantum confinement. The transition from indirect to direct band gap, the large exciton binding energy, and the strong photo-luminescence (PL) resulting from the absence of interlayer coupling plus the lack of inversion symmetry have been observed.[2−7] Particularly, TMDs such as monolayer WSe$_2$, MoS$_2$, and WS$_2$ with direct band gaps of about 1.65, 1.80, and 2.00 eV,[2,3,5] respectively, are highly flexible[8] and transparent,[2,7] making them promising candidates for ultrathin, flexible, and transparent optoelectronic devices, such as solar cells, photo-detectors, and light-emitting devices operating in the visible

range, as well as the displays and wearable electronics. Additionally, inversion symmetry breaking can make the electronic states of the two valleys have different chiralities and further introduce contrasting circular dichroism in different k-space regions, that is, the transitions at K and K′ points are allowed for σ$^+$ and σ$^−$ circularly polarized light, respectively.[9−14] Including the freedom of valley polarization, a novel valley light emitting diode (LED) has been proposed to obtain the circularly polarized light.[15]

As known, the p−n junction is the typical building block for LED, where electroluminescence (EL) can be realized by radiative transition between the electrons and holes electrically injected from n- and p-type semiconductors, respectively. So far, the EL of exfoliated monolayer MoS$_2$ has been observed
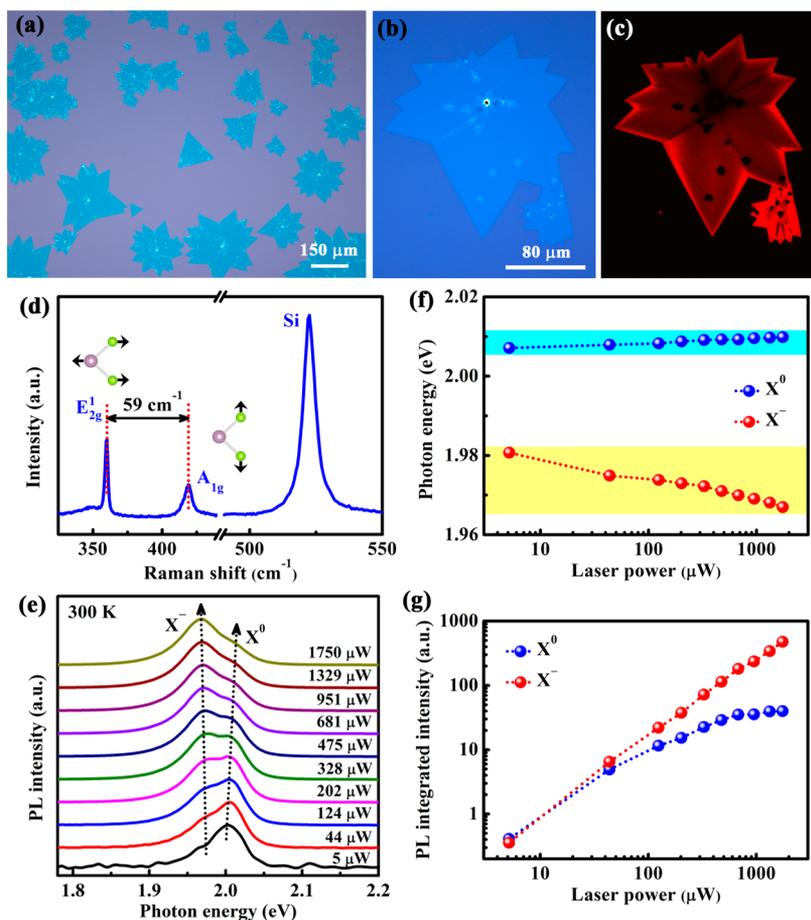
Figure 1. Characterization of CVD-grown WS_2 at room temperature. (a,b) Optical images of as-grown WS_2 on SiO_2/Si substrate. (c) Fluorescence image of the starlike WS_2 flake shown in the optical image of (b). (d) Raman spectra of as-grown WS_2 excited by 488 nm laser. (e) Normalized power-dependent photoluminescence spectra of as-grown WS_2 monolayer excited by 532 nm laser. (f) Photon energies of the neutral exciton X^0 and the negative trion X^- as a function of excitation power. (g) Dependence of integrated intensities of the neutral exciton X^0 and the negative trion X^- on excitation power.

both in a metal-MoS_2 Schottky junction via a hot carrier process[16] and the p−n heterojunction formed by using heavily p-doped Si and natural n-type MoS_2.[17,18] Meanwhile, LEDs based on exfoliated monolayer WSe_2 and WS_2 have been realized by creating lateral p−n homojunction in which the junction is formed electrostatically within the same layer by applying two independent gate voltages to in-plane adjacent regions.[19−22] However, the EL that creates through hot carrier process and in the p−n heterojunction is localized in the region adjacent to the electrical contacts and at the edge of the heterojunction, respectively. Meanwhile, the space charge distribution resulted from the electrostatic doping is usually inhomogeneous due to the fringe electrical field. Compared with the conventional LEDs and OLEDs, the gate voltages applied for the electrostatic doping cost extra energy consumption. Additionally, the circularly polarized EL of MoS_2, $MoSe_2$, and WSe_2 has been realized by Zhang et al. due to valley overlap polarization (VOP) induced by forward bias.[23] However, the circularly polarized EL of monolayer WS_2 has not been realized yet. More importantly, the previously used MoS_2, WSe_2, and WS_2 in LEDs[16−22] are all only a few micrometer-size exfoliated flakes with randomly distributed thicknesses and orientations. These monolayer diodes are not suitable for large-scale lighting device fabrication because the micromechanical exfoliation technique is unfavorable for good

control over the area and thickness of the film. Such limitations can be overcome by large-area grown TMDs with high crystal quality and uniformity. Recently, large-area growth of MoS_2, WSe_2, and WS_2 monolayers by chemical vapor deposition (CVD) method has been reported.[24−26] We also have reported the growth of large-area WS_2 monolayers with size up to hundreds of micrometers and high optical quality by a customized CVD system.[27] Here, we report the electrically tunable EL from CVD-grown monolayer WS_2 with optional intensity, energy, and valley polarization by constructing the p−i−n heterojucntion.

The used monolayer WS_2 samples were grown on cleaned 300 nm SiO_2/Si wafers by CVD method via the direct sulfurization of WO_3 powders as reported previously.[27] Figure 1a shows the optical image of our CVD-grown WS_2 flakes on SiO_2/Si substrate. Most of the flakes present starlike structures up to hundreds of micrometers in size. The samples are further characterized by fluorescence (FL) microscopy, Raman, and PL measurements at room temperature to rapidly analyze the layer number, uniformity, and quality of the WS_2 flakes. Figure 1b,c illustrates the optical and FL images of one typical WS_2 flake. The WS_2 flake shows strong red luminescence, resulting from the direct exciton emission. Raman and power-dependent PL spectra were excited by 488 and 532 nm lasers, respectively. Two prominent Raman peaks, in-plane E^1_{2g} and out-of-plane
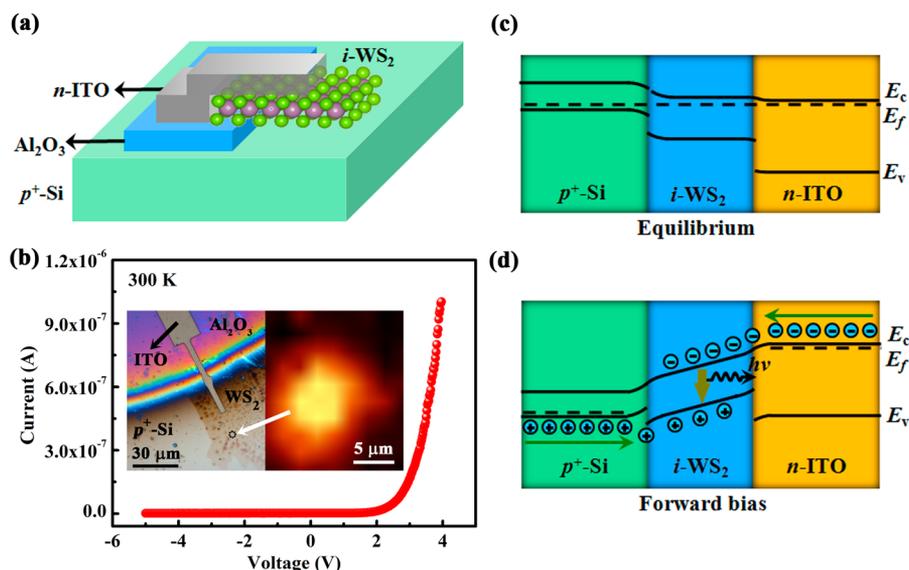
Figure 2. Geometry and electrical characteristic of the LED device. (a) Schematic of the p^+-Si/i-WS$_2$/n-ITO heterojunction LED device. (b) Room-temperature $I-V$ characteristic of the p^+-Si/i-WS$_2$/n-ITO heterojunction LED. Inset shows the high-magnification optical images of the LED device and EL mapping image as the white arrow indicated. (c,d) Band diagram of the p^+-Si/i-WS$_2$/n-ITO heterojunction in equilibrium condition and under forward bias, respectively. Electrons injected from the n-ITO and holes from p^+-Si can radiatively recombine in the intrinsic WS$_2$ monolayer.

A_{1g} modes, were observed at 360 and 419 cm^{-1}, respectively (see Figure 1d). The difference between E^1_{2g} and A_{1g} modes ($\Delta\omega = 59$ cm^{-1}) agrees with others' reports for either chemically synthesized or physically exfoliated monolayer WS$_2$.[3,6,27] These observations indicate the monolayer nature of the CVD-grown WS$_2$ flakes.

Figure 1e illustrates the normalized PL spectra of as-grown monolayer WS$_2$ as a function of the excitation power at room temperature. The overall emission profile evolves from the single peak at 2.003 eV under low excitation powers to the two-component completing feature under middle excitation powers, and finally to a single emission peak at 1.968 eV under high excitation powers. The higher energy emission assigned to the neutral exciton X^0 dominates the spectra obtained under low powers, while the lower one becomes dominant under high powers and is attributed to the negative trion X$^-$. To further reveal the response of netural exciton and negative trion to photoexcitation, we fitted the spectra with two Lorentzian components. Their emission energies and integrated intensities are plotted as functions of the excitation power (see Figure 1f,g). As the excitation power increases, the peak position of X^0 slightly blueshifts while that of X$^-$ apparently redshifts. Consequently, the energy difference between X^0 and X$^-$ increases, which is strongly related to phase space blocking[28] and manybody effects.[29] The slight blueshift of X^0 here is attributed to the reduction of the exciton binding energy with the increasing electron doping induced by photoexcitation,[30] while the redshift of X$^-$ is due to increase in the dissociation energy of trion[31] caused by the photon-induced rise of Fermi level. With the increasing excitation power, the emission profile broadens toward the lower photon energies due to the strengthening of the trion emission component and its redshift; the integrated intensity of X$^-$ is weaker than that of X^0 at lower excitation and increases linearly, while that of X^0 sublinearly increases at lower excitation powers (<681 μW) and saturates at higher excitation powers (>681 μW), resulting in a switch of the emission profile from the neutral exciton to the negative trion. The rising intensity ratio of X$^-$/X^0 versus neutral exciton

energy (see Figure S1) agrees well with the previous result[30] and is mainly caused by the photoinduced electron doping.

The as-obtained and intrinsic WS$_2$ monolayer was further used to fabricate the LED devices. Different from the reported LED structure based on the p−i−n homojunction formed by fabricating an electric-double-layer transistor (EDLT),[23] we constructed a p^+-Si/i-WS$_2$/n-ITO heterojucntion in which heavily p-doped Si and n-ITO are adopted to inject holes and electrons into i-WS$_2$, respectively, as shown in Figure 2a. The 300 nm thick Al$_2$O$_3$ is used as the insulating layer to prevent the direct contact between p^+-Si and n-ITO. Considering that ITO is a transparent and highly conductive n-type oxide,[32] it is introduced as both the electron-injecting layer and the electrode. $I-V$ characteristic of the device was measured at room temperature in vacuum, as shown in Figure 2b. The inset of Figure 2b shows the high-magnification optical image of one final fabricated LED device and the EL image. Also, Figure S2 shows the low-magnification optical images of the different LED devices that we fabricated. It is found that EL emission occurs within one region in the vicinity of ITO electrode. The $I-V$ characteristic clearly exhibits well rectifying behavior with low leakage current in the reverse bias, indicating that the p−i−n heterojunction is formed. The LED device is turned on at about 2 V. Although a rather high ideality factor of 15.7 is extracted from the forward $I-V$ characteristic by using the diode equation and taking the series resistance of the device into account,[33] the current reaches 1 μA when the applied forward bias is increased to 4 V. High ideality factors have been reported in GaN-based p−n diodes and AlGaN/InGaN LEDs and such values imply that the tunneling mechanism dominates the carrier transport rather than diffusion or recombination process.[34−37]

Figure 2c,d illustrates the band diagrams of the p^+-Si/i-WS$_2$/n-ITO heterojunction under the equilibrium condition and the forward bias, respectively. In equilibrium, there is a large valence band offset of 1.23 eV between p^+-Si and monolayer WS$_2$ due to their different band gaps and electron affinities.[38,39] When the heterojunction is forward biased, the holes from p^+-Si

are injected into monolayer WS$_2$, and the larger valence band offset between monolayer WS$_2$ and ITO forms a barrier to block the injected holes from leaking into the n-type layer. The electrons and holes injected from the ITO layer and p$^+$-Si, respectively, can give rise to efficient radiative recombination in the monolayer WS$_2$, resulting in light emission.

To enhance the EL efficiency, the current-dependent EL measurements were carried out at 77 K unless otherwise specified. Figure 3a depicts the representative EL spectra
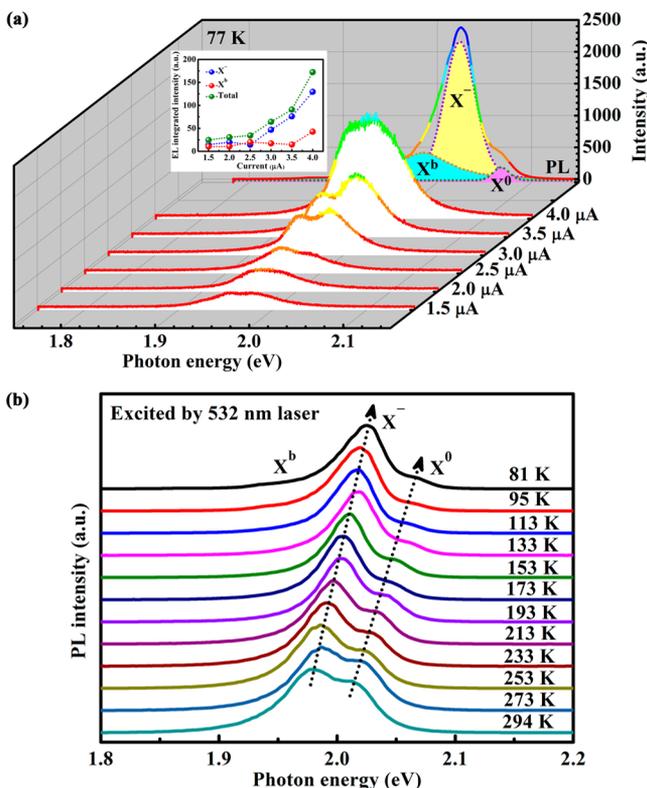

Figure 3. Current-dependent electroluminescence and temperature-dependent photoluminescence spectra of the LED device. (a) Electroluminescence spectra of the LED device recorded at 77 K under different injection current, varying from 1.5 to 4.0 μA. The multiple colors in each individual curve represent the luminescence intensity. The data can be well fitted with two Lorentzian functions, which are assigned to the negative trion X$^-$ and bound exciton X^b by comparing with the below photoluminescence spectrum obtained at 81 K. Inset: Integrated intensities of the negative trion X$^-$ and bound exciton X^b versus injection current extracted from the current-dependent electroluminescence spectra. (b) Normalized temperature-dependent photoluminescence spectra of the LED device excited by 532 nm laser.

obtained under varied currents. As shown in Figures 3a and S3, the emission with two main peaks at 1.950 and 1.985 eV, respectively, can be observed at an injection current of 1.5 μA. As the current increases, both emission components get stronger and the EL spectra present the striking feature of competition between them. In order to clarify the emission peaks that appeared in the EL spectra, the temperature-dependent PL measurements were also performed over the temperature range from 81 to 294 K, as shown in Figure 3b. For comparison, the PL spectrum collected at 81 K is also shown in Figure 3a, accompanied by the fitting with three peaks. As the temperature decreases to 81 K, X$^-$ and X^0

blueshift to 2.024 and 2.068 eV, respectively. Meanwhile, the emission component located at a lower energy 1.985 eV becomes much more obvious at the lower energy shoulder of X$^-$. Note that the broad emission that can be attributed to defect-induced bound excitons (X^b) often appears for monolayer TMDs at low temperature or in vacuum.[40,41] Hence, the temperature-dependent PL measurements can also be used to get further insight into the structural defects of monolayer TMDs. For CVD-grown monolayer WS$_2$ used in our device, X^b is much weaker than X$^-$ and does not appear as a dominant emission at low temperature, suggesting few structural defects or impurities in our CVD-grown monolayer WS$_2$. On the basis of the temperature-dependent PL spectra, two emission bands that appear in the low-current EL spectra with positions of 1.950 and 1.985 eV (see Figure S3), matching well with the observed X^b and X$^-$ in the PL spectra at low temperature, are assigned to defect-induced bound exciton and trion, respectively. Compared with the PL spectrum at 81 K, the obtained EL spectra show a redshift due to the rise of local temperature induced by the electrical bias.

We further extract quantitative information on current-dependent EL spectra by fitting the data with Lorentzian functions corresponding to X^b and X$^-$. Their emission energies and integrated intensities as functions of the injection current are plotted in Figure S4 and inset of Figure 3a, respectively. As the injection current increases, the peak positions of both X^b and X$^-$ remain stable. At the low injection current, the integrated intensity of X^b is comparable with that of X$^-$ because the carriers are frozen out onto defects at low temperature. When the current increases from 2.5−4.0 μA, injection of carriers into the WS$_2$ leads to more formation of negatively charged excitons, whereas the defects are almost fully occupied with excitons. As a result, the integrated intensity of X$^-$ increases much more rapidly than that of X^b and X$^-$ starts to dominate the EL spectrum, where the band realignment probably takes responsibility. This is consistent with the result that X$^-$ increases more rapidly than X^b and keeps increasing while X^b exhibits saturation behavior as the laser power increases at 81 K (see Figure S5). As shown in Figure 2d, with the increase in the forward bias the conduction band offset at the interface between i-WS$_2$ and n-ITO favors the injection of electrons while the valence band offset at the interface between p$^+$-Si and i-WS$_2$ tends to impede injection of holes. As a result, the imbalanced carrier injection under the forward bias results in the enhanced n-type doping, that is, the rise of Fermi level, and thus enhances the negative trion emission. These data clearly show that the dominant component emission of EL from CVD monolayer WS$_2$ can be controlled by the injection current. The result that X$^-$ dominates the EL under the high injection current is in agreement with the observation of stronger X$^-$ than other excitonic emissions in the PL spectra at low temperature.

Another feature that the EL from the p$^+$-Si/i-WS$_2$/n-ITO heterojunction LED shows net circular polarization is also clearly observed. This is the first demonstration of circularly polarized EL from the CVD grown monolayer WS$_2$. The current-dependent circularly polarized EL spectra normalized to the right handed circular (σ$^+$) component at each injection current are shown in Figure 4a. The degree of circular polarization, defined as $\eta = [I(\sigma^+) - I(\sigma^-)]/[I(\sigma^+) + I(\sigma^-)]$, where $I(\sigma^+)$ and $I(\sigma^-)$ are the integrated intensities of σ$^+$ and σ$^-$ circularly polarized EL components, respectively, is plotted in Figure 4b,c. For this device, the right-handed circularly
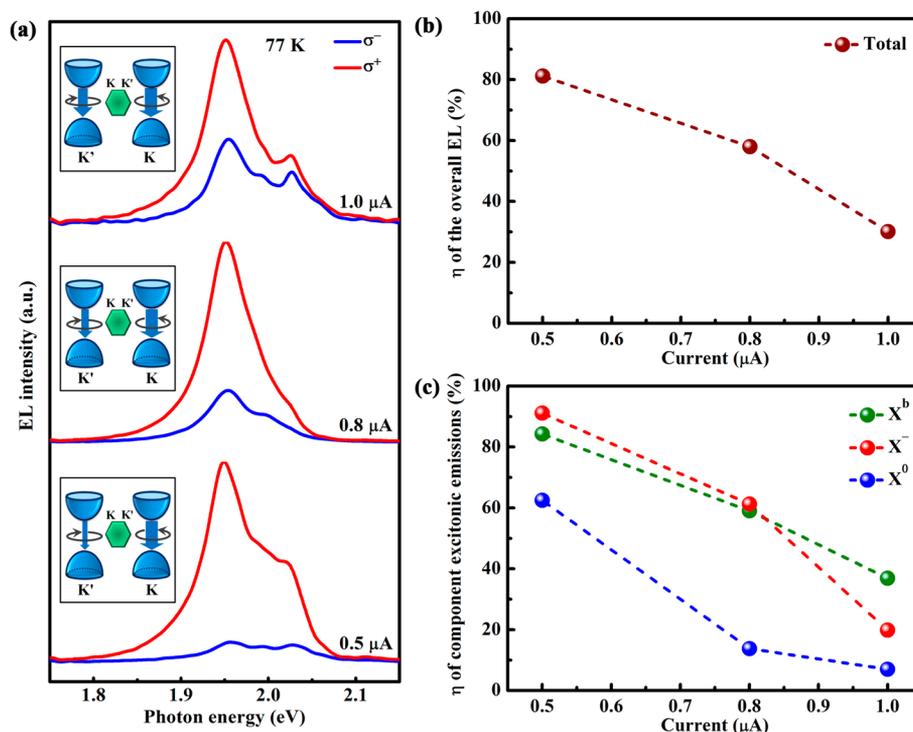
Figure 4. Circularly polarized electroluminescence of the LED device at 77 K. (a) The current-dependent circularly polarized electroluminescence spectra normalized to the right handed circular (σ^+) component at each injection current. Inset: Schematic illustration of valley-contrasting circular dichroism under different current injection. (b,c) Current dependence of the degree of circularly polarized electroluminescence for the overall emission and component netural exciton X^0, negative trion X^-, and bound exciton X^b extracted from panel a.

polarized EL component σ^+ is stronger than the left one σ^-. As shown in Figure 4b, the degree of circular polarization of the total EL reaches as high as 81% at 0.5 μA, which is much larger than those of exfoliated WSe_2, $MoSe_2$, and MoS_2 reported by Zhang et al.[23] Also, it drastically decreases to 30% as the injected current increases to 1.0 μA, which is quite different from the result that η has the smaller current dependence shown in ref 23. The circularly polarized EL spectra can be fitted by three Lorentizian components (see Figure S6), which are assigned to X^0, X^-, and X^b, respectively. All three components show the similar degradation of polarization with the increasing forward current while the larger net circular polarization degrees have been found for X^- and X^b than that of X^0. These circularly polarized behaviors will be further discussed later. Our result demonstrates that the degree of circular polarization can be modulated simply by the injection current. In view of the practical device applications, this is very encouraging and also superior to that modified by different circularly polarized laser excitation energy and power,[13,14,42,43] as well as temperature.[13,14]

Here, electrically tunable valley-LED has been demonstrated by use of CVD-grown monolayer WS_2. Superior to the exfoliated samples used in recently reported TMD-based LEDs[16−22] for practical applications, the active emitting 2D semiconductor in our case is CVD-grown, which is highly compatible with extensively used large-scale device integration technology. Note that, the similar circularly polarized EL has previously been observed in the spin-LEDs and spin-OLEDs.[44−49] However, the emission mechanism and the environmental surrounding of the valley-LEDs are quite different from those of the spin-LEDs and spin-OLEDs. In particular, the typical spin-LEDs requires both injection of spin-

polarized carriers from magnetic materials and operation under magnetic field in order to observe the circularly polarized EL, where the polarization sign is typically switched by changing the direction of magnetic field.[44,45] In the case of spin-OLEDs, metamaterials or chiral polymers are required and the circular polarization is fixed with a specific material configuration.[46−49] In contrast, the valley polarization of EL from our valley-LEDs is strongly related to the valley asymmetry at K and K′ (i.e., different electron−hole overlap) resulted from the build-in electric field. The degree of circular polarization can be effectively modulated by the forward current injection without need of magnetic field and magnetic elements or chiral molecules. The sign switching of valley polarized EL can be realized by adjusting the direction of applied forward bias relative to the crystal orientation, which has been demonstrated by employing multiple electrodes.[23] Remarkably, the emission components and polarization of EL are electrically tunable. The dominant emission component can vary among neutral exciton, trion, and bound exciton species when the prepared p−i−n heterostructure is under a forward bias. For example, the band realignment with the applied bias can affect the injection of electrons and holes, which can be used to manipulated the doping-sensitive charged exciton emission.

The valley polarization of EL from our LED can be understood in terms of different electron−hole overlap at K and K′ valleys, which are induced by the build-in potential associated with carrier injections[23] and the presence of valley polarized two-dimensional electron gas (2DEG) with the carrier injection.[50] On the one hand, according to the semiclassical transport theory, Zhang et al. have proposed a model of valley overlap polarization (VOP) to explain the circularly polarized luminescence induced by electrical injection

into TMDs that possess two isolated anisotropic valleys with different chiralities, where two key factors are carrier distribution and build-in electric field.[23] In particular, carrier distributions in TMDs are intrinsically anisotropic due to trigonal warping.[51] Under the effect of build-in electric field, electron and hole distributions shift toward opposite directions, respectively, which introduce different overlaps of electron−hole distributions in the momentum space between the two valleys nearby K and K′.[23] As a result, the unequal electron−hole overlap causes different luminescence intensities from two valleys and finally leads to circularly polarized EL. In our case, out-of-plane bias may exist in the device. To our best knowledge, for 2D materials there is very limited information on the out-of-plane resistance in contrast to the in-plane resistance, which makes the precise determination of the bias drop in the vertical direction unattainable. Considering the ultrathin thickness in the vertical direction (<1 nm), the finite out-of-plane resistivity and the relatively large cross-sectional area, the typical out-of-plane resistance is much lower than the in-plane resistance. As a result, the vertical bias drop is negligible compared to the one caused by the in-plane resistance at the certain current. Thus, we consider that the in-plane bias plays the predominant role in the chiral EL. As shown in Figure 2d, under the forward bias, the electrons and holes from n-type ITO and p^+-type Si, respectively, are injected into the middle layer where the build-in potential appears within monolayer WS_2. Such a build-in potential shifts anisotropic carrier distributions at K and K′ and thus results in chiral EL. Note that although p−i−n LED structures are formed differently here and in ref 23 (that is, by use of hetero- and homojunctions, respectively), the emission mechanism of the chiral EL from the middle layer is similar in principle. On the other hand, more recently Scrace et al. have suggested that strong Coulomb interaction and locking of spin and valley degrees of freedom due to spin orbit coupling can cause the valley polarized 2DEG and further result in the net circular polarization of the trion emission.[50] In our case, the presence of the similar 2DEG can account for the observed valley-dependent X^- component with a larger polarization degree than that of X^0 in the EL spectra. Note that the valley polarization can be affected by several factors, such as current density, the direction of build-in electric field, build-in potential, carrier scattering, and emission components. Here, the observed decrease of the circular polarization degree with the increasing current is mainly attributed to the rising K↔K′ intervalley scattering with the increasing doping.[13,14,42] The reduced polarization degree in MoS_2 has been observed with the increasing intervalley scattering,[42] which is consistent with our argumentation above. Besides, the bias-induced doping itself in WS_2 has no apparent effect on the observed changes of circular polarization degree, which is supported by recent electrically gated measurements on MoS_2[52] and WS_2[14] devices.

In summary, we report the electrically tunable and circularly valley-LED by constructing the p−i−n heterojucntion of p^+-Si/CVD-grown i-WS_2/n-ITO. The fabricated device shows classic rectification resulted from the formation of p−i−n hetero-junction. By injecting the forward current, EL from CVD-grown monolayer WS_2 was obtained successfully and the excitonic emission from CVD-grown monolayer WS_2 was tunable by varying the injection current. On the other hand, the EL spectra show the net circular polarization. The degree of circular polarization reaches as high as 81% and can be also modulated by the applied current. Our demonstration of EL

from CVD-grown monolayer WS_2 paves the way for large-scale fabrication of the light-emitting device based on atomically thin TMDs. The electrically tunable and circularly polarized light from the light-emitting devices open up new opportunities for the emerging valley-based optoelectronics.

Methods. *Sample Growth and Device Fabrication.* The used monolayer WS_2 samples were grown on cleaned 300 nm SiO_2/Si wafers by CVD method via the direct sulfurization of WO_3 powders as reported in ref 27. Then, the as-obtained intrinsic WS_2 monolayer was further used to fabricate the LED devices by constructing a p−i−n heterojunction. First, an array consisting of Al_2O_3 circular truncated cone with a thickness of 300 nm and a diameter of 600 μm was deposited on p^+-Si by an electron-beam evaporation deposition system using the copper hard mask. Then, WS_2 monolayers can be placed across the p^+-Si/Al_2O_3 step and contact with p^+-Si naturally after wet transfer followed by annealing. The monolayer WS_2 flakes across the edges of the circular truncated cones were chosen to further fabricate the device. The 220 nm thick ITO layer was patterned by electron-beam lithography (EBL) and followed by an electron-beam evaporation deposition and the lift-off of the PMMA photoresist by acetone.

Optical and Electrical Measurements. The optical and fluorescence images were taken by an Olympus fluorescence microscope equipped with a mercury lamp. The fabricated LEDs based on the p^+-Si/i-WS_2/n-ITO heterojunction were bonded to a printed circuit board (PCB) attached to a three-dimensional piezo-stage in a WITec confocal micro-Raman/PL spectroscopic system equipped with a liquid-nitrogen cryostat. Lasers of 488 and 532 nm were used as the excitation sources for the Raman and PL measurements, respectively, through a 50× objective lens and the signals were collected by a grating (2400/mm and 600/mm, respectively) spectrometer with a thermoelectrically cooled detector. The power-dependent PL measurements were conducted at room temperature in vacuum ($\sim 1 \times 10^{-5}$ mBar). The excitation power on samples was tuned in the range from 0 to 1750 μW. The laser spot size on samples is ~ 1 μm. The temperature-dependent PL measurements were performed by combined use of the WITec system and Linkam optical DSC600 stage equipped with the T95-Linksys PC interface controller and LNP95 cooling system with liquid nitrogen. I−V characteristic and current injecting for the EL measurements of the LEDs in vacuum were conducted by using the Keithley 4200-SCS semiconductor characterization system. The quarter-wave plate converts the circularly polarized light (σ^+/σ^-) into the linear polarized light (parallel/perpendicular to the polarizer). By rotating the polarizer by 90° with a fixed angle of the wave plate, each circular EL component was selectively measured.

■ ASSOCIATED CONTENT

Ⓢ Supporting Information

The Supporting Information is available free of charge on the ACS Publications website at DOI: 10.1021/acs.nano-lett.5b04066.

> The rising integrated intensity ratio of X^-/X^0 versus photon energy of X^0 from the CVD-grown WS_2. The low- and high-magnification optical images of different LED devices. The fitting of the typical EL and circularly polarized EL spectra, as well as the information extracted from the current-dependent EL and circularly polarized EL spectra measured at 77 K. The power-dependent PL

spectra of the LED device excited by 532 nm laser at 81 K, together with the power dependence of extracted intensity for the negative trion X^- and bound exciton X^b. (PDF)

■ AUTHOR INFORMATION

Corresponding Authors
*E-mail: YuTing@ntu.edu.sg.
*E-mail: iamwhuang@njtech.edu.cn.

Author Contributions
W.Y. and J. S. contributed equally.

Notes
The authors declare no competing financial interest.

■ ACKNOWLEDGMENTS

■ REFERENCES

(1) Wang, Q. H.; Kalantar-Zadeh, K.; Kis, A.; Coleman, J. N.; Strano, M. S. *Nat. Nanotechnol.* **2012**, *7*, 699.

(2) Mak, K. F.; Lee, C.; Hone, J.; Shan, J.; Heinz, T. F. *Phys. Rev. Lett.* **2010**, *105*, 136805.

(3) Zhao, W.; Ghorannevis, Z.; Chu, L.; Toh, M.; Kloc, C.; Tan, P.-H.; Eda, G. *ACS Nano* **2013**, *7*, 791.

(4) Zeng, H.; Liu, G.-B.; Dai, J.; Yan, Y.; Zhu, B.; He, R.; Xie, L.; Xu, S.; Chen, X.; Yao, W.; Cui, X. *Sci. Rep.* **2013**, *3*, 1608.

(5) Splendiani, A.; Sun, L.; Zhang, Y.; Li, T.; Kim, J.; Chim, C.-Y.; Galli, G.; Wang, F. *Nano Lett.* **2010**, *10*, 1271.

(6) Gutiérrez, H. R.; Perea-López, N.; Elías, A. L.; Berkdemir, A.; Wang, B.; Lv, R.; López-Urías, F.; Crespi, V. H.; Terrones, H.; Terrones, M. *Nano Lett.* **2013**, *13*, 3447.

(7) Tonndorf, P.; Schmidt, R.; Böttger, P.; Zhang, X.; Börner, J.; Liebig, A.; Albrecht, M.; Kloc, C.; Gordan, O.; Zahn; Dietrich, R. T.; De Vasconcellos, S. M.; Bratschitsch, R. *Opt. Express* **2013**, *21*, 4908.

(8) Bertolazzi, S.; Brivio, J.; Kis, A. *ACS Nano* **2011**, *5*, 9703.

(9) Zeng, H.; Dai, J.; Yao, W.; Xiao, D.; Cui, X. *Nat. Nanotechnol.* **2012**, *7*, 490.

(10) Mak, K. F.; He, K.; Shan, J.; Heinz, T. F. *Nat. Nanotechnol.* **2012**, *7*, 494.

(11) Cui, X. *Proc. of SPIE* **2013**, *8813*, 88132H-1.

(12) Cao, T.; Wang, G.; Han, W.; Ye, H.; Zhu, C.; Shi, J.; Niu, Q.; Tan, P.; Wang, E.; Liu, B.; Feng, J. *Nat. Commun.* **2012**, *3*, 887.

(13) Yan, T.; Qiao, X.; Tan, P.; Zhang X. arXiv preprint arXiv:1502.07088, 2015.

(14) Zhu, B.; Zeng, H.; Dai, J.; Gong, Z.; Cui, X. *Proc. Natl. Acad. Sci. U. S. A.* **2014**, *111*, 11606.

(15) Yao, W.; Xiao, D.; Niu, Q. *Phys. Rev. B: Condens. Matter Mater. Phys.* **2008**, *77*, 235406.

(16) Sundaram, R. S.; Engel, M.; Lombardo, A.; Krupke, R.; Ferrari, A. C.; Avouris, Ph.; Steiner, M. *Nano Lett.* **2013**, *13*, 1416.

(17) Ye, Y.; Ye, Z.; Gharghi, M.; Zhu, H.; Zhao, M.; Wang, Y.; Yin, X.; Zhang, X. *Appl. Phys. Lett.* **2014**, *104*, 193508.

(18) Lopez-Sanchez, O.; Alarcon Llado, E.; Koman, V.; Fontcuberta i Morral, A.; Radenovic, A.; Kis, A. *ACS Nano* **2014**, *8*, 3042.

(19) Ross, J. S.; Klement, P.; Jones, A. M.; Ghimire, N. J.; Yan, J.; Mandrus, D. G.; Taniguchi, T.; Watanabe, K.; Kitamura, K.; Yao, W.; Cobden, D. H.; Xu, X. *Nat. Nanotechnol.* **2014**, *9*, 268.

(20) Baugher, B. W. H.; Churchill, H. O. H.; Yang, Y.; Jarillo-Herrero, P. *Nat. Nanotechnol.* **2014**, *9*, 262.

(21) Pospischil, A.; Furchi, M. M.; Mueller, T. *Nat. Nanotechnol.* **2014**, *9*, 257.

(22) Jo, S.; Ubrig, N.; Berger, H.; Kuzmenko, A. B.; Morpurgo, A. F. *Nano Lett.* **2014**, *14*, 2019.

(23) Zhang, Y. J.; Oka, T.; Suzuki, R.; Ye, J. T.; Iwasa, Y. *Science* **2014**, *344*, 725.

(24) Liu, K.-K.; Zhang, W.; Lee, Y.-H.; Lin, Y.-C.; Chang, M.-T.; Su, C.-Y.; Chang, C.-S.; Li, H.; Shi, Y.; Zhang, H.; Lai, C.-S.; Li, L.-J. *Nano Lett.* **2012**, *12*, 1538.

(25) Huang, J.-K.; Pu, J.; Hsu, C.-L.; Chiu, M.-H.; Juang, Z.-Y.; Chang, Y.-H.; Chang, W.-H.; Iwasa, Y.; Takenobu, T.; Li, L.-J. *ACS Nano* **2014**, *8*, 923.

(26) Song, J.-G.; Park, J.; Lee, W.; Choi, T.; Jung, H.; Lee, C. W.; Hwang, S.-H.; Myoung, J. M.; Jung, J.-H.; Kim, S.-H.; Lansalot-Matras, C.; Kim, H. *ACS Nano* **2013**, *7*, 11333.

(27) Cong, C.; Shang, J.; Wu, X.; Cao, B.; Peimyoo, N.; Qiu, C.; Sun, L.; Yu, T. *Adv. Opt. Mater.* **2014**, *2*, 131.

(28) Zhang, C.; Wang, H.; Chan, W.; Manolatou, C.; Rana, F. *Phys. Rev. B: Condens. Matter Mater. Phys.* **2014**, *89*, 205436.

(29) Hawrylak, P. *Phys. Rev. B: Condens. Matter Mater. Phys.* **1991**, *44*, 3821.

(30) Shang, J.; Shen, X.; Cong, C.; Peimyoo, N.; Cao, B.; Eginligil, M.; Yu, T. *ACS Nano* **2015**, *9*, 647.

(31) Mak, K. F.; He, K.; Lee, C.; Lee, G. H.; Hone, J.; Heinz, T. F.; Shan, J. *Nat. Mater.* **2012**, *12*, 207.

(32) Chopra, K. L.; Major, S.; Pandya, D. K. *Thin Solid Films* **1983**, *102*, 1.

(33) Neamen, D. A. *Semiconductor Physics and Devices: Basic Principles*, 3rd ed; McGraw-Hill: New York, 2003, 269.

(34) Casey, H. C.; Muth, J., Jr.; Krishnankutty, S.; Zavada, J. M. *Appl. Phys. Lett.* **1996**, *68*, 2867.

(35) Perlin, P.; Osińsky, M. P.; Eliseev, G.; Smagley, V. A.; Mu, J.; Banas, M.; Sartori, P. *Appl. Phys. Lett.* **1996**, *69*, 1680.

(36) Dmitriev, V. A. *MRS Internet J. Nitride Semicond. Res.* **1996**, *1*, 29.

(37) Deb, P.; Kim, H.; Qin, Y.; Lahiji, R.; Oliver, M.; Reifenberger, R.; Sands, T. *Nano Lett.* **2006**, *6*, 2893.

(38) Tan, S. T.; Sun, X. W.; Zhao, J. L.; Iwan, S.; Cen, Z. H.; Chen, T. P.; Ye, J. D.; Lo, G. Q.; Kwong, D. L.; Teo, K. L. *Appl. Phys. Lett.* **2008**, *93*, 013506.

(39) Ballif, C.; Regula, M.; Lévy, F. *Sol. Energy Mater. Sol. Cells* **1999**, *57*, 189.

(40) Kobayashi, Y.; Sasaki, S.; Mori, S.; Hibino, H.; Liu, Z.; Watanabe, K.; Taniguchi, T.; Suenaga, K.; Maniwa, Y.; Miyata, Y. *ACS Nano* **2015**, *9*, 4056.

(41) Tongay, S.; Suh, J.; Ataca, C.; Fan, W.; Luce, A.; Kang, J. S.; Liu, J.; Ko, C.; Raghunathanan, R.; Zhou, J.; Ogletree, F.; Li, J.; Grossman, J. C.; Wu, J. *Sci. Rep.* **2013**, *3*, 2657.

(42) Kioseoglou, G.; Hanbicki, A. T.; Currie, M.; Friedman, A. L.; Gunlycke, D.; Jonker, B. T. *Appl. Phys. Lett.* **2012**, *101*, 221907.

(43) Lagarde, D.; Bouet, L.; Marie, X.; Zhu, C. R.; Liu, B. L.; Amand, T.; Tan, P. H.; Urbaszek, B. *Phys. Rev. Lett.* **2014**, *112*, 047401.

(44) Žutić, I.; Fabian, J.; Das Sarma, S. D. *Rev. Mod. Phys.* **2004**, *76*, 323.

(45) Chen, J. Y.; Ho, C. Y.; Lu, M. L.; Chu, L. J.; Chen, K. C.; Chu, S. W.; Chen, W.; Mou, C. Y.; Chen, Y. F. *Nano Lett.* **2014**, *14*, 3130.

(46) Jeong, S. M.; Ohtsuka, Y.; Ha, N. Y.; Takanishi, Y.; Ishikawa, K.; Takezoe, H.; Nishimura, S.; Suzaki, G. *Appl. Phys. Lett.* **2007**, *90*, 211106.

(47) Zinna, F.; Giovanella, U.; Bari, L. D. *Adv. Mater.* **2015**, *27*, 1791.

(48) Yang, Y.; da Costa, R. C.; Smilgies, D. M.; Campbell, A. J.; Fuchter, M. J. *Adv. Mater.* **2013**, *25*, 2624.

(49) Konishi, K.; Nomura, M.; Kumagai, N.; Iwamoto, S.; Arakawa, Y.; Kuwata-Gonokami, M. *Phys. Rev. Lett.* **2011**, *106*, 057402.

(50) Scrace, T.; Tsai, Y.; Barman, B.; Schweidenback, L.; Petrou, A.; Kioseoglou, G.; Ozfidan, I.; Korkusinski, M.; Hawrylak, P. *Nat. Nanotechnol.* **2015**, *10*, 603.

(51) Kormányos, A.; Zólyomi, V.; Drummond, N. D.; Rakyta, P.; Burkard, G.; Fal'ko, V. I. *Phys. Rev. B: Condens. Matter Mater. Phys.* **2013**, *88*, 045416.

(52) Wu, S.; Ross, J. S.; Liu, G.-B.; Aivazian, G.; Jones, A.; Fei, Z.; Zhu, W.; Xiao, D.; Yao, W.; Cobden, D.; Xu, X. *Nat. Phys.* **2013**, *9*, 149.